Liquid Processing of Bismuth–Silica Nanoparticle/Aluminum Matrix Nanocomposites for Heat Storage Applications

Binghua Ma, Walid Baaziz, Léo Mazerolles, Ovidiu Ersen, Bernard Sahut, Clément Sanchez, Stéphane Delalande, David Portehault

Liquid Processing of Bismuth–Silica Nanoparticle/Aluminum Matrix Nanocomposites for Heat Storage Applications

Binghua Ma, Walid Baaziz, Léo Mazerolles, Ovidiu Ersen, Bernard Sahut, Clément Sanchez, Stéphane Delalande,* and David Portehault*

Metal matrix nanocomposites encompassing low-melting point metal nano-inclusions are promising candidates for thermal regulation of devices at high temperature. They are usually processed by solid-state routes that provide access to a limited range of materials and are hardly compatible with complex shaping processes and with large-scale applications. Herein, we develop a liquid-phase processing technique to design aluminum matrix nanocomposites made of phase change nanoparticles, using bismuth nanoparticles as a proof-of-concept. The bismuth nanoparticles derived from colloidal chemistry are first encapsulated in a silica shell and then dispersed by ultrasonication into molten aluminum. Using X-ray diffraction, electron microscopy, and X-ray photoelectron spectroscopy, we probe the evolution of the bismuth particles and of the inorganic shell. We demonstrate that the silica shell acts as a barrier against extensive coalescence of particles during the dispersion process, thus enabling a decrease and a widening of the phase change temperature range.

aluminum, composites, nanoparticles, core–shell, bismuth, heat storage, phase change

INTRODUCTION

Phase change materials (PCMs) display a promising range of applications for thermal control of electronic devices[1] and for flame retardants[2−4] by absorbing and releasing heat upon melting and solidifying, respectively. Compared to air and liquid cooling or to heat pipes, PCMs use less power and require less complex thermal system design.[5] Enhancing the heat management efficiency of PCMs and their response time requires a significant increase in their thermal conductivity.[6] This aim can be reached by embedding phase change inclusions within metal matrices that are much more thermally conductive than common polymer matrices and also offer higher mechanical strength.[6] The development of composites made of metallic PCM inclusions into metallic matrices would provide access to temperature ranges that are not accessible to organic PCMs,[7] thus paving the way to other fields of applications, such as the automotive field. Using PCM metal or alloy nanoparticles and their related depression of melting point versus bulk materials would offer an additional degree of freedom by enabling to tune the phase change temperature (PCT) not only with the composition but also with the particle size.[8] These metal matrix nanocomposites are, however, limited by their fabrication. To ensure dispersion of the inclusions, they are produced either by powder metallurgy[9,10] or by chemical synthesis of the matrix,[8] which are not adapted to large-scale applications.[9] Dispersion of PCM nanoscaled inclusions into metal matrices by liquid metallurgy would offer access to a wide range of materials with high versatility in the choice of the materials and of the PCT. It would also enable coupling with a variety of liquid-based shaping processes and would deliver materials relevant at the industrial scale. However, the targeted PCTs are usually below the melting point of the metal matrix. Therefore, producing metal matrix PCM nanocomposites by liquid metallurgy is a great challenge as it means dispersing liquid metal droplets in another liquid metal, at temperatures usually above 600 °C, while avoiding coalescence of the PCM inclusions and/or alloying with the matrix. Melt spinning has been proposed to quench the coalescence of particles precipitated in the liquid phase by fast cooling when the matrix is an amorphous alloy.[11] The method cannot be applied to bulk crystalline matrices. As a result, no crystalline metal matrix PCM composite, containing either nano- or micro-inclusions, has been reported from liquid metallurgy processes.

To address this challenge and enable liquid processing of metallic phase change nanocomposites, we propose to disperse colloidal chemistry-derived metal PCM nanoparticles in a

molten metal by using ultrasonication[12] in the melt at high temperatures (Figure 1, pathway A). To enhance the

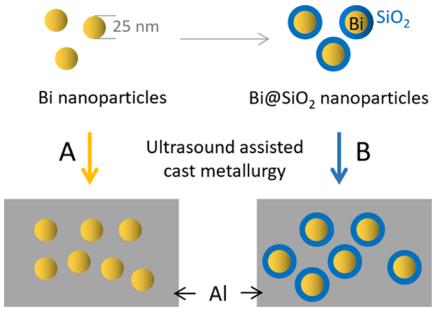

Figure 1. Scheme of the synthesis procedure for aluminum nanocomposites embedding Bi nanoparticles and Bi@SiO_2 core@shell nanoparticles. Pathways A and B correspond to the ultrasound-assisted incorporation of Bi and Bi@SiO_2 nanoparticles, respectively.

dispersion and the stability over thermal cycling of the nanoparticles (Figure 1, pathway B), we encapsulate them in a silica shell prior to incorporation into the liquid metal. During incorporation, the shell is expected to react *in situ* with the metal matrix through the aluminothermal reduction.[13] We study herein the evolution of this shell, its impact on the nanostructure of the nanocomposites and on their phase change energy storage properties. We show that this procedure provides sustainable phase change properties over thermal cycling by maintaining the nanosize of the metal cores. We use bismuth nanoparticles as proof-of-concept phase change inclusions for their low-melting point and aluminum as a light weight, high thermal conductivity matrix.

RESULTS AND DISCUSSION

Synthesis and Characterization of Bi@SiO_2 Nanostructures. We have prepared bismuth nanoparticles according to the colloidal synthesis proposed by Scheele et al.[14] where bismuth acetate was reduced in oleylamine to form bismuth nanoparticles with 1-dodecanethiol ligands. X-ray diffraction (XRD) confirms (Figure S1) the formation of bismuth, and transmission electron microscopy (TEM) (Figure 2a) shows that the particles exhibit a narrow size distribution centered at around 25 nm. In the second step, the bismuth nanoparticles were coated with a silica shell by adapting the Stöber method to ensure heterogeneous nucleation at the surface of the particles.[15,16] TEM indicates a 7 nm thick shell with a contrast lower than the bismuth core (Figure 2b). The silica shell actually embeds several particles, forming aggregates with size up to 160 nm. The dispersion state within the aggregates was quantified by the projected area distribution (Figure 2c), which shows that the silica shells embed from single to about 20 bismuth cores. Although significant aggregation is observed, the dispersion state is enhanced compared to previous methods using surfactants,[17] instead of strongly bound thiol surface ligands.

To evaluate the efficiency of the silica shell in preventing coalescence of the bismuth cores, we have heated the core–shell nanostructures and sole bismuth nanoparticles above the melting point of bulk Bi (271 °C). When heated at 320 °C, the bare Bi particles undergo extensive coalescence and growth (Figure S2). On the contrary, the general appearance of the Bi@SiO_2 nanostructures was preserved at 350 °C (Figure 2d), and the size of the Bi cores only slightly increased for the cores

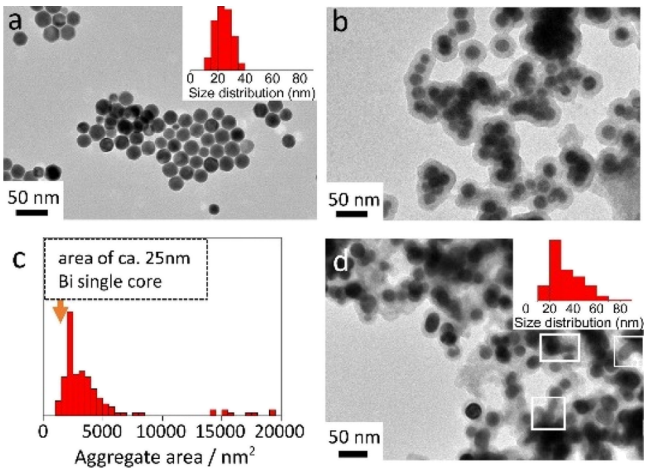

Figure 2. (a) TEM image and size distribution of Bi nanoparticles. (b) TEM image and (c) core projected area distribution of Bi@SiO_2 nanostructures. (d) TEM image and size distribution of Bi@SiO_2 nanostructures heated at 350 °C. The white squares are showing areas where coalescence of the cores occurred within silica shells.

embedded in the same silica shell. Thus, the silica shell preserves the separated Bi cores from coalescence.

To provide additional information on coalescence during heating and cooling, *in situ* TEM experiments were carried out on Bi@SiO_2 nanostructures by heating to 350 °C at 10 °C min^{-1}. Scanning transmission electron microscopy–high-angle annular dark-field imaging (STEM–HAADF) images (Figure S3) show that the morphology of the nanoparticles was retained during heating and cooling, with a contrast revealing the clear edge of overlapped nanoparticles. The dependency of the coalescence behavior versus the aggregation state inside the silica shells has been further studied by *in situ* TEM (Figure S4). Above the melting point of Bi cores at around 250 °C, Bi cores embedded in the same silica shell and in contact with each other coalesce irreversibly (Figure S4, orange rectangle), while Bi cores initially separated with a silica layer from each other remain dispersed upon heating and cooling. Although Bi cores initially embedded together coalesce, they still remain trapped inside the shell over the melting point, thus making feasible the incorporation of Bi@SiO_2 nanostructures into molten aluminum.

Bi@SiO_2–Al Nanocomposites. Nanocomposites made of an aluminum matrix embedding Bi@SiO_2 (Bi@SiO_2–Al) were synthesized by ultrasound-assisted liquid metallurgy. To ensure the full incorporation of the nanoparticles into molten aluminum, a pellet of Bi@SiO_2 nanostructures (0.25 at %) in aluminum was prepared by pressing Bi@SiO_2 and aluminum powders pre-dispersed into ethanol (see details in the experimental method section). The pellet was then incorporated into molten aluminum at 740 °C by ultrasound treatment in an induction furnace. The resulting samples showed metallic aluminum appearance (Figure S5). The Bi/Al ratio was evaluated by wavelength-dispersive X-ray fluorescence spectrometry (WDXRF) on the top and bottom of each sample and on middle slice cuts of the monoliths. The constant ratio of 0.3 at % in all pieces is consistent with the initial precursor ratio, indicating that all the nanostructures were incorporated and are homogeneously distributed into the whole volume of the monoliths.

Scanning electron microscopy (SEM) imaging in the backscattered electron mode (Figure 3a) highlights white

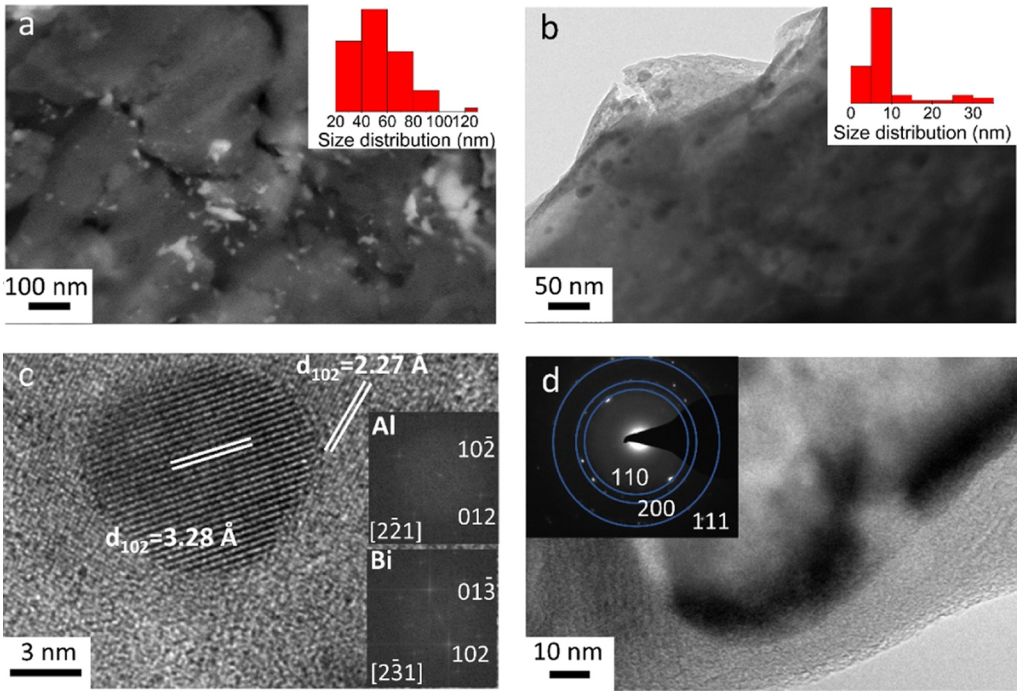

Figure 3. SEM and TEM study of a Bi@SiO_2−Al nanocomposite. (a) Backscattered electron imaging-mode SEM image, bright and dark areas correspond to Bi and Al regions, respectively. (b−d) TEM images. Dark and light contrasts correspond to Bi and Al, respectively. Insets in (a,b) show the corresponding size distributions. The inset in (d) shows the SAED pattern corresponding to image (d) and indexed along the structure of bismuth.

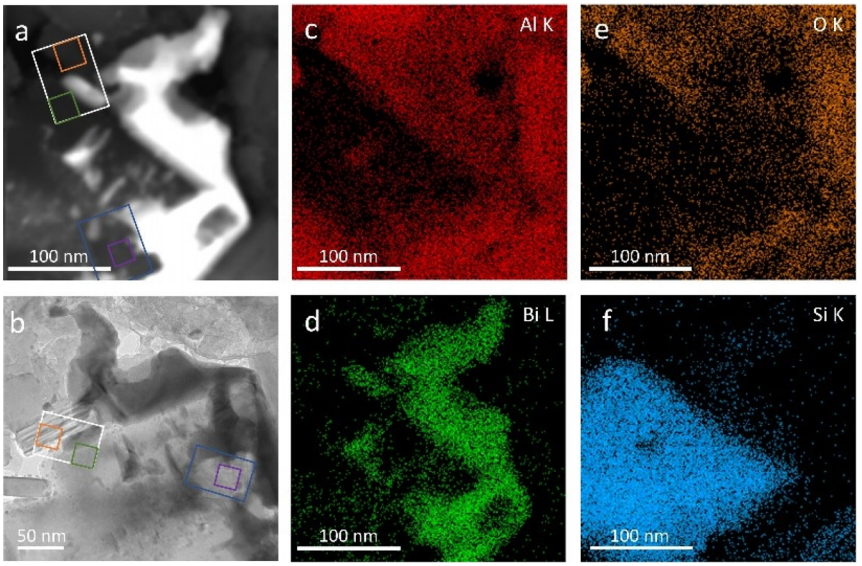

Figure 4. (a) STEM−HAADF, (b) STEM images, and corresponding (c−f) STEM−EDS maps of Bi@SiO_2−Al nanocomposites.

areas corresponding to electron-rich bismuth, with a size up to 120 nm. The TEM images reveal 10 nm (Figure 3b,c) and 60 nm (Figure 3d) bismuth nanoparticles, well crystallized in the Bi hexagonal structure according to high-resolution TEM (HRTEM) (Figure 3c inset) and selected area electron diffraction (SAED) (Figure 3d inset) performed on the larger particles. HRTEM (Figure 3c) also highlights atomic planes of the Al matrix and does not indicate any intermediary phase between the matrix and the nanoparticles. Larger particles around 120 nm were also observed by STEM−HAADF (Figure S6). The size distributions evaluated by SEM and TEM highlight two distinct populations, centered, respectively, at *ca.* 60 and 8 nm. According to TEM, particles below 10 nm were isotropic, while the shape of particles above 30 nm was irregular. Therefore, SEM and TEM evidence a widening of the size distribution from initial 25 nm Bi nanoparticles toward both smaller and larger particles. This behavior is indicative of Ostwald ripening during the incorporation process, a phenomenon in which bismuth from the smaller particles dissolve in the liquid medium and redeposit on larger particles. This hypothesis is supported by the slight but significant solubility of Bi in Al at 700 °C of about 1.5 wt %.[18] Note that sonication may also exacerbate Ostwald ripening, as already described on polymer composites.[19,20]

An area containing a large coalesced bismuth object was mapped by the STEM−energy-dispersive system (EDS) (Figure 4a−f). Bi was surrounded by an O-rich area also containing Al but exempt of Si (orange square, Figure 4a). This area corresponds (orange square, Figure 5a,b) to an Al/O-rich rod-like region with non-uniform contrast, which highlights crystal defects. The interplanar distances measured by HRTEM are consistent with Al_2O_3 (100) planes. Therefore, bismuth is surrounded by alumina.

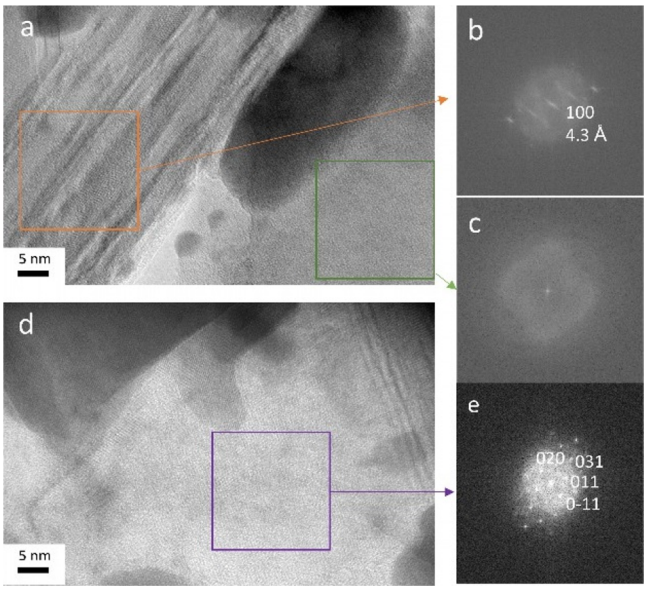

Figure 5. HRTEM study of the areas highlighted in Figure 4a,b by white, green, and violet squares. (a) HRTEM image acquired in the white rectangle in Figure 4a,b. (b,c) Fast Fourier transforms (FFTs) corresponding to the orange and green squares in (a) and in Figure 4a,b. The FFT in (b) for the Al/O-rich area is indexed along the structure of α-Al_2O_3. The FFT in (c) for the Si-rich area shows an amorphous region. (d) HRTEM image shown in the blue rectangle in Figure 4a,b. (e) FFT of the violet area in (d), indexed along the structure of Al_2SiO_5.

The Si map (Figure 4f) confirms that silicon was no longer around Bi particles and segregated into Bi-free areas (Figures 4 and 5a green square, 5d violet square). The low overlap between Si-rich and O-rich regions (Figure 4f,e) indicates the formation of low oxidation state silicon species. We observed two types of regions in Si-rich area: an amorphous-like (Figure 5a green square and 5c) region and a crystalline region (Figures 5d violet square and 5e). HRTEM analysis and the corresponding FFT of the crystalline part (Figure 5e) are fully consistent with the structure of sillimanite Al_2SiO_5. We discuss below the origin of these different components, which are indicative of the reaction mechanisms occurring during incorporation of the nanoparticles into the aluminum melt.

The presence of alumina, low oxidation state silicon species, and the aluminosilicate sillimanite is consistent with aluminothermic reduction of the silica shell of the Bi@SiO_2 nanostructures, yielding aluminosilicates as reaction intermediates.[13] In order to further confirm this reaction pathway, the redox processes involving the aluminum matrix and the silica shell were probed on a slice cut piece of nanocomposites analyzed by X-ray photoelectron spectroscopy (XPS) in the Si 2p (Figure 6a) and Si 2s (Figure 6b) regions. The spectrum of pure aluminum was also recorded as a reference. The Al

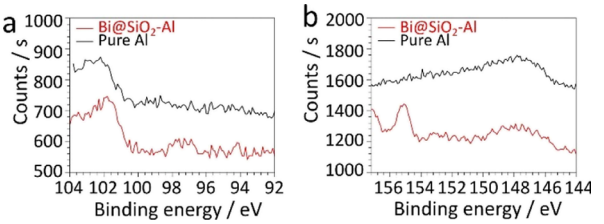

Figure 6. XPS analysis of Bi@SiO_2−Al nanocomposites (red) and pure Al (black) at the (a) Si 2p and (b) Si 2s areas.

plasmonic peak overlaps with the Si 2p binding energy regions between 99 and 102 eV (Figure 6a), but the Si 2s area enables to decipher the Al plasmon peak at 147.4 eV from the Si 2s signal at about 150−155 eV (Figure 6b). For the Bi@SiO_2−Al composite, the most intense peak at 155.1 eV accounts for the Si−O bonds of SiO_2.[21] An additional contribution between 150 and 154 eV is not observed for pure aluminum and is ascribed to other silicon species at lower binding energy than that for SiO_2, which is consistent with low oxidation state Si species and/or an aluminosilicate.[13] According to XPS and STEM−EDS (Figures 4a,b and 5), we assign the amorphous areas to low oxidation state silicon. Because oxidation of low oxidation state Si species could occur upon exposure to air during transfer of the sample to the XPS chamber, the pristine samples could exhibit a higher portion of reduced silicon than indicated by XPS analysis.

The reduction of SiO_2 particles (about 30 μm) by molten aluminum has been studied by Deqing and Ziyuan.[13] In the Al−SiO_2 system, the reduction of silica by aluminum is thermodynamically favorable (reaction 1 below). Once alumina is formed, it can react with remaining silica and then form mullite or other aluminosilicates (reaction 2), evolving finally toward alumina and silicon (reaction 3).

$$4Al + 3SiO_2 \rightarrow 2Al_2O_3 + 3Si \quad (1)$$

$$3Al_2O_3 + 2SiO_2 \rightarrow Al_6Si_2O_{13} \quad (2)$$

$$8Al + 3Al_6Si_2O_{13} \rightarrow 13Al_2O_3 + 6Si \quad (3)$$

Deqing and Ziyuan[13] also observed the formation of a 5 μm thick shell of alumina surrounding unreacted ~20 μm silica particles after 30 min of reaction at 700 with 5 °C min^{-1} heating rate, while silicon had migrated within the aluminum matrix and formed rod-like Si inclusions. In our study, the silica component is present in the silica shell with a thickness of 7 nm, 3 orders of magnitude lower than previously studied,[13] which supports the reduction of silica to a larger extent at a similar temperature. Nonetheless, aluminothermic reduction is not complete as we observe, besides amorphous low oxidation state silicon, an intermediate Si(IV)-containing aluminosilicate. This behavior can be attributed to short reaction times, as our experiments rely on induction heating at a rate of 350 °C min^{-1} and reaction time of 10 min. We have observed the formation of sillimanite (Al_2SiO_5) as the intermediate phase. Generally, sillimanite forms above 776 °C,[22] corresponding to 40 °C over our synthesis temperature. This high-temperature phase may be induced by intense local heating provided by ultrasound treatment.[23]

Overall, we propose the following reaction mechanism: Bi nanoparticles were partially coalesced inside the silica shell during the heating ramp. The pristine silica shell was reduced by aluminum that is concomitantly oxidized and reacts with

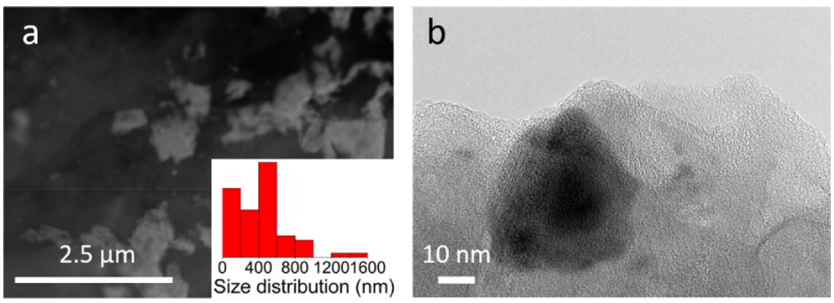

Figure 7. (a) SEM image and corresponding size distribution and (b) TEM image of a Bi–Al nanocomposite.

remaining silica to form an aluminosilicate intermediate. During ultrasound-assisted heating for the nanocomposite preparation, the silica shell separates from the Bi core, leading to a leaching of Bi droplets which then undergo Ostwald ripening and develop into two populations.

Bi–Al Nanocomposites. To probe the impact of the silica shell on the dispersion of Bi nano-objects, we have incorporated Bi nanoparticles without silica into molten aluminum, as described above for $Bi@SiO_2$–Al composites. The as-obtained Bi–Al composite exhibits also an evolution of Bi objects into two populations (Figure 7), one around one micrometer and another one around 5–30 nm. Bismuth then underwent Ostwald ripening, as with the silica shell, but the population of large objects showed significantly larger size, losing the nanoscale, when no silica was used. Therefore, although the silica shell in $Bi@SiO_2$–Al composites underwent chemical reaction and local mobilization, it acted efficiently against coalescence of the cores during incorporation into molten aluminum. Thus, the $Bi@SiO_2$–Al nanocomposite exhibited a wide size distribution at the nanoscale.

Thermal Properties of Bismuth and $Bi@SiO_2$ Nanoparticles. Differential scanning calorimetry (DSC) was performed for both precursor Bi, $Bi@SiO_2$ nanoparticles, and the corresponding nanocomposites. Figure 8a,b displays the

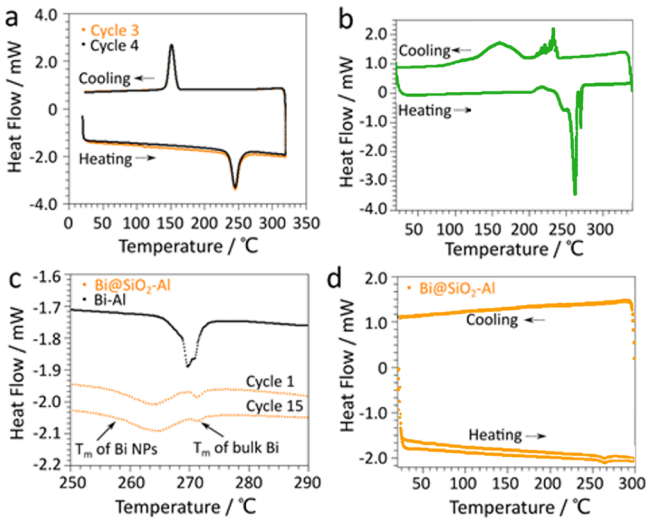

Figure 8. DSC analysis of (a) $Bi@SiO_2$ during the third heating–cooling cycle and of (b) Bi nanoparticles (green). (c, d) DSC analysis of a $Bi@SiO_2$–Al nanocomposite with (c) zoomed-in area at 250–290 °C during heating for the 1st and 15th cycles (orange). The DSC analysis of a reference Bi–Al sample is also shown for the first heating ramp in (c) (black).

thermal behavior at the third heating–cooling cycle for pristine $Bi@SiO_2$ and Bi nanoparticles, respectively. $Bi@SiO_2$ particles exhibit an endothermic peak at ~242 °C, which is in agreement with the depression of the melting point (271 °C for bulk Bi) with particle size decrease.[8] The melting point measured herein for 25 nm silica-coated Bi nanoparticles is in accordance with the results obtained for Bi-carbon nanocomposites.[24] $Bi@SiO_2$ nanoparticles exhibit reversible thermal properties over four cycles (Figure 8a). On the contrary, the bare bismuth nanoparticles (Figure 8b) display three sharp endothermic peaks at ~263 and 271 °C, the latter corresponding to bulk Bi melting. The first two endothermic peaks are attributed to the melting temperature depression with the particle size.[8] The appearance of the peaks at higher temperature indicate that the nanoparticles coalesced, and large particles up to bulk were formed. Therefore, the silica shell was necessary to maintaining the nanoscale and the melting point depression of Bi nanostructures. These results are consistent with TEM observations after heating (Figure S2).

Thermal Properties of Nanocomposites Encompassing Phase Change Bismuth Inclusions. The DSC curves for the $Bi@SiO_2$–Al composites (Figure 8c,d) also show endothermic peaks during heating and an exothermic broad peak during cooling, indicating solidification of undercooled bismuth. The high-temperature region of the DSC curves (Figure 8c) shows that the melting behavior significantly differs from those of the initial particles described above. The $Bi@SiO_2$–Al nanocomposite exhibits two endothermic peaks: a broad melting peak at 263 °C with the onset temperature at 251 °C, corresponding to nanoparticles melting, and a low intensity sharper peak at 271 °C, corresponding to bulk bismuth. The shift of these peaks to higher temperatures compared to unreacted $Bi@SiO_2$ nanoparticles confirms that the nanoparticles coalesced during the incorporation of the particles into the melt, but a significant fraction still shows melting point depression, indicating that nanoscale objects have been maintained. This is consistent with the remaining single Bi nanoparticles or aggregates of only few Bi cores within the initial nanocomposite, as described above (Figures 3 and S6). The enthalpy ratio for the peaks at 263 and at 271 °C is 9:1, indicating that around 90% of Bi element are still nanoscaled, with the assumption that the melting latent heat of nanoscale Bi is close to the value for bulk Bi. Because the melting latent heat decreases with the particle size,[8] one can assume that the molar fraction of bismuth at the nanoscale is above 90%. The heat absorption ability evaluated by the enthalpy of the melting process was 0.38 J g^{-1}, close to the expected value based on the chemical composition at 0.47 J g^{-1} using the melting latent heat of bulk Bi. DSC over 15

consecutive heating−cooling cycles between 20 and 300 °C showed the cycling ability of the Bi core after melting as the DSC curves and the latent heat remained unchanged during cycling. The silicon species are considered stable after cycling as the aluminosilicate phases are stable,[25] and no reaction is expected between Al and Bi[26] on the one side and Al and Si[27] on the other side. Besides, thermal cycling is performed at temperatures much lower than the preparation temperature in molten aluminum, so that any structural changes are unlikely.

The heat absorption ability of the as-prepared Bi@SiO_2−Al nanocomposite is low compared to Bi@Al_2O_3−Al prepared by powder metallurgy[28] because we used a low Bi content material as a proof-of-concept. The heat storage capacity may be improved by increasing the amount of inclusion particles within the matrix. We did not detect by DSC the phase change of small nanoparticles around 8 nm expected from TEM observations, which occurred at around 240 °C in an Ag matrix.[8] This could be explained by the decreased enthalpy with the particle size[14,29] or the low volume fraction of nanoparticles smaller than 10 nm. DSC further confirms the efficient role of the silica shell to limit the coalescence of Bi nanoparticles since the Bi−Al nanocomposite showed three endothermic peaks at 262, 269, and 271 °C overlapped together and shifted to higher temperature compared to the Bi@SiO_2−Al nanocomposite, which implies the consecutive coalescence of nanoparticles into bulk objects during cycling.

Compared to a Bi−Al composite prepared by powder metallurgy[10] at the same heating rate and with micron and nano-sized bismuth inclusions, the distribution of melting temperatures for Bi@SiO_2−Al prepared by our liquid metallurgy process is broader and shifted to lower temperatures. This demonstrates a decreased Bi particle size achieved through nanoparticle encapsulation. The small initial nanoparticle size, the protective silica shell, the ultrasound treatment inducing disruption of Bi droplets, and the rapid thermal treatments by induction heating are keys to achieve small inclusion nanoparticles with a wide phase transition temperature range, which can be a considerable advantage to ensure progressive heat absorption over a wide temperature range.

CONCLUSIONS

We have developed an ultrasound-assisted liquid metallurgy process to phase change metal matrix nanocomposites, by encapsulating pre-made metal nanoparticles within a silica shell. This shell acts as a barrier against extensive coalescence of the metal cores, which are molten during the incorporation process. This process relies on preliminary synthesis of nanoparticles, which ensures the suitability of the method for the very wide range of metal and alloy nanomaterials accessible by rich colloid chemistry. Hence, we believe that the process opens the way to a wide diversity of lightweight aluminum-based phase change materials that could be shaped according to liquid metal processing. Therefore, various fields of application can be targeted, including thermal regulation in automobiles. We also expect the mechanical properties of the resulting nanocomposites to be influenced by phase change inclusions. This point will be addressed in the future.

EXPERIMENTAL METHODS

Materials. Bismuth acetate (99.99%), oleylamine (technical grade, 70%), 1-dodenanethiol (98%), tetraethyl orthosilicate (TEOS, 99.99%), ammonia aqueous solution (28−30%), and aluminum powder (99.99%, 320 mesh) were all purchased from Sigma-Aldrich. Aluminum beads (99.9%, around 3 mm diameter) were obtained from Alfa Aesar. The reagents were used as received.

Synthesis of Bismuth Nanoparticles and Silica-Coated Bismuth Nanoparticles. Bismuth nanoparticles were prepared by colloidal synthesis in a mixture of organic solvents based on a previous published protocol.[14] Bismuth acetate (1 mmol) was mixed with 1-dodecanethiol (11.1 mL) and heated to 45 °C for 45 min under vacuum. The reaction flask was purged with N_2 and heated to 60 °C. Oleylamine (22.2 mL) at room temperature was quickly added under stirring, and the reaction mixture was further heated for 24 h. Finally, Bi nanoparticles were washed two times by ethanol/chloroform (20/1 vol/vol) and re-dispersed in ethanol. The silica-coated bismuth nanoparticles were prepared according to the Stöber method as follows:15 TEOS was dissolved in absolute ethanol at a concentration of 0.38 M. 10 μL of TEOS solution and 100 μL of ammonia 30% were subsequently added to the 1 mL of alcoholic bismuth suspension [Bi] = 6×10^{-4} M under vigorous stirring. The mixture was heated at 40 °C for 3 h followed by washing by two cycles of centrifugation-redispersion in ethanol. The final powder was dried in a vacuum oven at 40 °C for 16 h. In order to evaluate the thermal stability, 20 mg of Bi@SiO_2 nanoparticles was annealed in a Naberthem chamber furnace under air condition for 1 h dwell time with a heating rate of 10 °C min^{-1}.

Synthesis of Bi−Al and Bi@SiO_2 Nanocomposites. Bi−Al nanocomposites were prepared by ultrasound-assisted casting of a mixture composed of nanoparticles and aluminum in an induction oven. Briefly, 2 g of aluminum powders and alcoholic bismuth suspension were mixed by sonication at the boiling point for 1 h to get a ratio of 0.3 at % between Bi and Al. Then, the mixture was dried in a vacuum oven at 40 °C for 1 h, followed by pressing into a 13 mm pellet under 8 tons for 2 min. Subsequently, the pellet and 0.4 g of pure Al beads were heated into an alumina crucible using an induction oven (CEIA, power cube 90 series 200) at 740 °C under an argon atmosphere. After dwelling for 1 min, an ultrasound power of 80 Watts (QSonica, Q500A-220, USA) was applied through a sonication horn (niobium tip with 4 mm diameter) to disperse the nanoparticles for 5 min. The final composite was obtained by cooling the melt in the crucible. It was then cut with a diamond wire saw for further analyses.

X-ray Diffraction. XRD was performed with a D8 Bruker diffractometer operating at the Cu Kα radiation in the Bragg Brentano configuration. The ICSD reference 64709 was used for the indexation of bismuth nanoparticles.

Electron Microscopy. The cut pieces of the samples were observed with SEM (Hitachi SU-70 microscope) equipped with an Oxford X-Max 50 mm^2 EDS detector. For preparation, the samples were mounted in polyfast resin (Struers), followed by a series of polishing steps through 1000, 2400, and 4800 grit papers (Buchler) and then with 3 and 1 μm diamond suspensions. For the observation of nanoparticles in TEM, the nanoparticles were dispersed in ethanol, and then, a drop was evaporated on a carbon-coated copper grid. For the composites, TEM thin films were prepared by a parallelepiped rectangle of 3 × 3 × 0.5 mm cut in the middle of the sample. Polishing was then performed with a diamond disk to get a 200 μm thick sample. The thickness of the center of the slab was further reduced to 50 μm using a precision dimpling instrument (model 515, South Bay Technology). Ion milling was performed for the final thinning. TEM images were recorded on a Tecnai spirit G2 microscope operating at 120 kV. The STEM images and STEM−EDX mapping were recorded with a JEM 2100Plus UHR microscope and a Tecnai F20 that were both operating at 200 kV. The size distribution of precursor nanoparticles was determined by counting 150−200 nanoparticles from TEM images. The size distribution of nanoparticles in the final nanocomposites was determined by counting 70−120 particles, from SEM images and TEM images, respectively. The ICDD 00380471 was used for the indexation of $AlSi_2O_5$.

Chemical Analysis by Wavelength-Dispersive X-ray Fluorescence Spectrometry. WDXRF spectroscopy was performed on

the cut pieces of the samples with a Bruker S8 Tiger spectrometer equipped with a Rh tube.

Differential Scanning Calorimetry. DSC analysis was performed in a TA Q20 DSC instrument. Around 10 mg of nanoparticles was sealed in an aluminum crucible. In the case of nanocomposites, top, middle, and bottom slices of the samples (around 40 mg) were analyzed separately to assess the homogeneity of the cast samples. To study the phase transition, the samples were heated to 320 °C and then cooled to 20 °C with a slope of 10 °C min^{-1} followed by 3 min of stabilization at 20 °C between each cycle. For each sample, at least three cycles were performed.

***In Situ* TEM.** The experiments were carried out using a JEOL JEM-2100F microscope operated at 200 kV equipped with a spherical aberration probe corrector (Cs from CEOS), high-resolution objective lens pole piece, and an UltraScan 1000 CCD array detector (GATAN). For *in situ* observations, a Protochips Atmosphere system was used. The samples were suspended between two micro-electro-mechanical system-based closed cells made up of transparent SiN_x (for observation) and SiC (for heating). The *in situ* observations were carried out at a pressure of 1 atm under Ar at a flow rate of 0.1 mL min^{-1}. The system was previously purged during few hours with the argon environment to ensure the proper cleaning of the gas lines and the sample holder.

AUTHOR INFORMATION

Corresponding Authors

Stéphane Delalande − *Stellantis, Centre Technique de Vélizy, route de Gisy, Vélizy-Villacoublay 78140, France*; Email: stephane.delalande@stellantis.com

David Portehault − *Sorbonne Université, CNRS, Collège de France, Laboratoire de Chimie de la Matière Condensée de Paris (LCMCP), F-75005 Paris, France;* orcid.org/0000-0003-4914-4913; Email: david.portehault@sorbonne-universite.fr

Authors

Binghua Ma − *Sorbonne Université, CNRS, Collège de France, Laboratoire de Chimie de la Matière Condensée de Paris (LCMCP), F-75005 Paris, France; Stellantis, Centre Technique de Vélizy, route de Gisy, Vélizy-Villacoublay 78140, France*

Walid Baaziz − *Université de Strasbourg, CNRS, Institut de Physique et Chimie des Matériaux de Strasbourg (IPCMS), 67034 Strasbourg cedex 2, France*

Léo Mazerolles − *Université Paris Est, CNRS, Institut de Chimie et des Matériaux Paris-Est (ICMPE), 94320 Thiais, France*

Ovidiu Ersen − *Université de Strasbourg, CNRS, Institut de Physique et Chimie des Matériaux de Strasbourg (IPCMS), 67034 Strasbourg cedex 2, France;* orcid.org/0000-0002-1553-0915

Bernard Sahut − *Stellantis, Centre Technique de Vélizy, route de Gisy, Vélizy-Villacoublay 78140, France*

Clément Sanchez − *Sorbonne Université, CNRS, Collège de France, Laboratoire de Chimie de la Matière Condensée de Paris (LCMCP), F-75005 Paris, France;* orcid.org/0000-0002-6426-4844

Author Contributions

B.M., D.P., B.S., S.D., and C.S. conceived the concept. B.M. performed synthesis, fabrication, and SEM and EDS characterization. L.M. prepared the TEM samples. W.B. and O.E. performed *in situ* TEM experiments. D.P. and S.D. supervised the project.

ACKNOWLEDGMENTS

The authors would like to thank for the funding by Stellantis and ANRT and the framework of the OpenLab $\beta\chi\Phi$ involving Stellantis and Sorbonne University. We thank the Institut des Matériaux de Paris Centre (IMPC FR2482) for servicing FEG-SEM, EDX and XPS measurements (David Montero, Antoine Miche), Laboratoire de Réactivité de Surface (UMR 7197) for servicing TEM (Patricia Beaunier), and Sorbonne Université, CNRS, and C'Nano projects of the Region Ile-de-France for funding.

REFERENCES

(1) Wu, M.-S.; Liu, K. H.; Wang, Y.-Y.; Wan, C.-C. Heat Dissipation Design for Lithium-Ion Batteries. *J. Power Sources* **2002**, *109*, 160−166.

(2) Qu, Z. G.; Li, W. Q.; Tao, W. Q. Numerical Model of the Passive Thermal Management System for High-Power Lithium Ion Battery by Using Porous Metal Foam Saturated with Phase Change Material. *Int. J. Hydrogen Energy* **2014**, *39*, 3904−3913.

(3) Alipanah, M.; Li, X. Numerical Studies of Lithium-Ion Battery Thermal Management Systems Using Phase Change Materials and Metal Foams. *Int. J. Heat Mass Transfer* **2016**, *102*, 1159−1168.

(4) Wu, W.; Yang, X.; Zhang, G.; Ke, X.; Wang, Z.; Situ, W.; Li, X.; Zhang, J. An Experimental Study of Thermal Management System Using Copper Mesh-Enhanced Composite Phase Change Materials for Power Battery Pack. *Energy* **2016**, *113*, 909−916.

(5) Offer, G.; Patel, Y.; Hales, A.; Diaz, L. B.; Marzook, M. Cool Metric for Lithium-Ion Batteries Could Spur Progress. *Nature* **2020**, *582*, 485−487.

(6) Jaguemont, J.; Omar, N.; Van den Bossche, P.; Mierlo, J. Phase-Change Materials (PCM) for Automotive Applications: A Review. *Appl. Therm. Eng.* **2018**, *132*, 308−320.

(7) Shchukina, E. M.; Graham, M.; Zheng, Z.; Shchukin, D. G. Nanoencapsulation of Phase Change Materials for Advanced Thermal Energy Storage Systems. *Chem. Soc. Rev.* **2018**, *47*, 4156−4175.

(8) Liu, M.; Ma, Y.; Wu, H.; Wang, R. Y. Metal Matrix-Metal Nanoparticle Composites with Tunable Melting Temperature and High Thermal Conductivity for Phase-Change Thermal Storage. *ACS Nano* **2015**, *9*, 1341−1351.

(9) Estruga, M.; Chen, L.; Choi, H.; Li, X.; Jin, S. Ultrasonic-Assisted Synthesis of Surface-Clean TiB_2 Nanoparticles and Their Improved Dispersion and Capture in al-Matrix Nanocomposites. *ACS Appl. Mater. Interfaces* **2013**, *5*, 8813−8819.

(10) Abraham, A.; Schoenitz, M.; Dreizin, E. L. Energy Storage Materials with Oxide-Encapsulated Inclusions of Low Melting Metal. *Acta Mater.* **2016**, *107*, 254−260.

(11) Goswami, R.; Chattopadhyay, K. Depression of Melting Point of Multidomained Bismuth in Aluminum Based Metallic Glass Nanocomposites. *Appl. Phys. Lett.* **1996**, *69*, 910−912.

(12) Mohanty, P.; Mahapatra, R.; Padhi, P.; Ramana, C. V. V.; Mishra, D. K. Ultrasonic Cavitation: An Approach to Synthesize

Uniformly Dispersed Metal Matrix Nanocomposites—A Review. *Nano-Struct. Nano-Objects* **2020**, *23*, 100475.
(13) Deqing, W.; Ziyuan, S. Aluminothermic Reduction of Silica for the Synthesis of Alumina-Aluminum-Silicon Composite. *J. Mater. Synth. Process.* **2001**, *9*, 241−246.
(14) Scheele, M.; Oeschler, N.; Meier, K.; Kornowski, A.; Klinke, C.; Weller, H. Synthesis and Thermoelectric Characterization of Bi_2Te_3 Nanoparticles. *Adv. Funct. Mater.* **2009**, *19*, 3476−3483.
(15) Wang, J.; Shah, Z. H.; Zhang, S.; Lu, R. Silica-Based Nanocomposites via Reverse Microemulsions: Classifications, Preparations, and Applications. *Nanoscale* **2014**, *6*, 4418−4437.
(16) Stöber, W.; Fink, A.; Bohn, E. Controlled Growth of Monodisperse Silica Spheres in the Micron Size Range. *J. Colloid Interface Sci.* **1968**, *26*, 62−69.
(17) Zhao, H.; Wang, J.; Li, X.; Li, Y.; Li, C.; Wang, X.; Wang, J.; Guan, S.; Xu, Y.; Deng, G.; Chen, Y.; Lu, J.; Liu, X. A Biocompatible Theranostic Agent Based on Stable Bismuth Nanoparticles for X-Ray Computed Tomography/Magnetic Resonance Imaging-Guided Enhanced Chemo/Photothermal/Chemodynamic Therapy for Tumours. *J. Colloid Interface Sci.* **2021**, *604*, 80−90.
(18) Manasijević, D.; Minić, D.; Balanović, L.; Premović, M.; Gorgievski, M.; Živković, D.; Milisavljević, D. Experimental Investigation and Thermodynamic Prediction of the Al−Bi−In Phase Diagram. *J. Alloys Compd.* **2016**, *687*, 969−975.
(19) Thompson, J. A.; Chapman, K. W.; Koros, W. J.; Jones, C. W.; Nair, S. Sonication-Induced Ostwald Ripening of ZIF-8 Nanoparticles and Formation of ZIF-8/Polymer Composite Membranes. *Microporous Mesoporous Mater.* **2012**, *158*, 292−299.
(20) Dirix, Y.; Bastiaansen, C.; Caseri, W.; Smith, P. Preparation, Structure and Properties of Uniaxially Oriented Polyethylene-Silver Nanocomposites. *J. Mater. Sci.* **1999**, *34*, 3859−3866.
(21) Barr, T. L. An XPS Study of Si as It Occurs in Adsorbents, Catalysts, and Thin Films. *Appl. Surf. Sci.* **1983**, *15*, 1−35.
(22) Salje, E. Heat Capacities and Entropies of Andalusite and Sillimanite: The Influence of Fibrolitization on the Phase Diagram of the Al_2SiO_5 Polymorphs. *Am. Mineral.* **1986**, *71*, 1366−1371.
(23) Suslick, K. S.; Didenko, Y.; Fang, M. M.; Hyeon, T.; Kolbeck, K. J.; McNamara, W. B.; Mdleleni, M. M.; Wong, M. Acoustic Cavitation and Its Chemical Consequences. *Philos. Trans. R. Soc. London* **1999**, *357*, 335−353.
(24) Tran, N.; Zhao, W.; Carlson, F.; Davidson, J. H.; Stein, A. Metal Nanoparticle − Carbon Matrix Composites with Tunable Melting Temperature as Phase-Change Materials for Thermal Energy Storage. *ACS Appl. Nano Mater.* **2018**, *1*, 1894−1903.
(25) Althaus, E. The Triple Point Andalusite — Sillimanite — Kyanite. *Contrib. Mineral. Petrol.* **1967**, *16*, 29−44.
(26) Medraj, A. M. Binary Phase Diagrams and Thermodynamic Properties of Silicon and Essential Doping Elements (Al, As, B, Bi, Ga, In, N, P, Sb and Tl). *Materials* **2017**, *10*, 676.
(27) Haghshenas, M.; Jamali, J. Assessment of Circumferential Cracks in Hypereutectic Al-Si Clutch Housings. *Case Stud. Eng. Fail. Anal.* **2017**, *8*, 11−20.
(28) Khan, Z.; Khan, Z.; Ghafoor, A. A Review of Performance Enhancement of PCM Based Latent Heat Storage System within the Context of Materials, Thermal Stability and Compatibility. *Energy Convers. Manage.* **2016**, *115*, 132−158.
(29) Fu, Q.; Zhu, J.; Xue, Y.; Cui, Z. Size- and Shape-Dependent Melting Enthalpy and Entropy of Nanoparticles. *J. Mater. Sci.* **2017**, *52*, 1911−1918.

Supporting information

Liquid Processing of Bismuth-Silica Nanoparticle/Aluminum Matrix Nanocomposites for Heat Storage Applications

Binghua Ma,[1,2] Walid Baaziz,[3] Léo Mazerolles,[4] Ovidiu Ersen,[3] Bernard Sahut,[2] Clément Sanchez,[1] Stéphane Delalande,[2] David Portehault[1]**

[1] Sorbonne Université, CNRS, Collège de France, Laboratoire de Chimie de la Matière Condensée de Paris (LCMCP), 4 place Jussieu, F-75005, Paris, France

[2] Stellantis, Centre Technique de Vélizy, route de Gisy, Vélizy-Villacoublay, 78140, France

[3] Université de Strasbourg, CNRS, Institut de Physique et Chimie des Matériaux de Strasbourg (IPCMS), 23 rue du Lœss BP 43, 67034 Strasbourg cedex 2, France

[4] Université Paris Est, CNRS, Institut de Chimie et des Matériaux Paris-Est (ICMPE), 2-8 rue H. Dunant, 94320, Thiais, France

*Corresponding authors:

david.portehault@sorbonne-universite.fr
stephane.delalande@stellantis.com

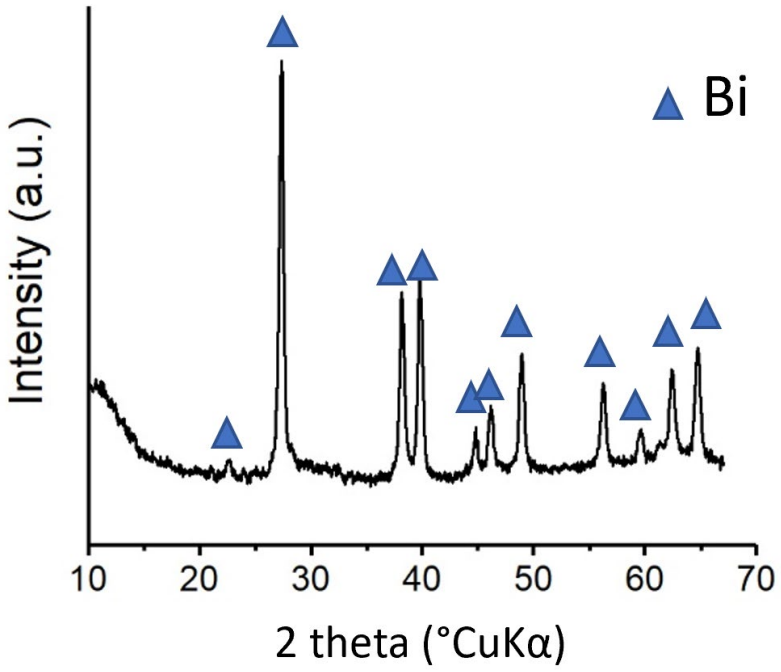

Figure S1. Powder XRD pattern of Bi nanoparticles.

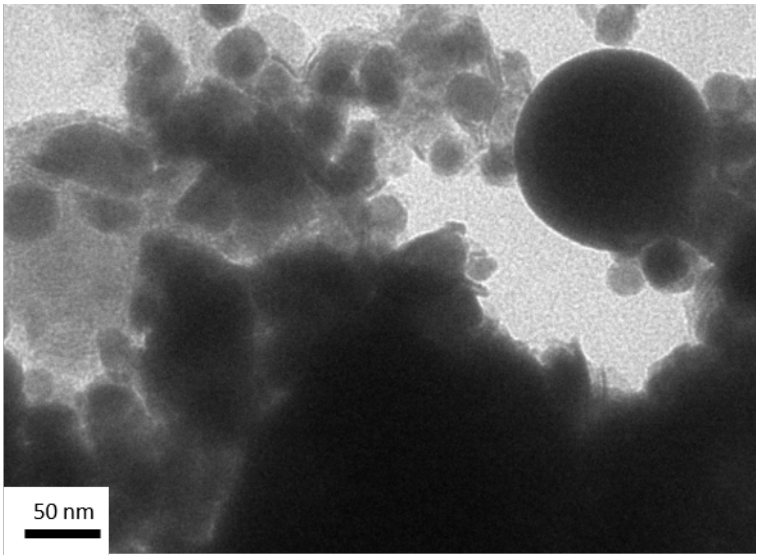

Figure S2. TEM image of bare Bi nanoparticles heated to 320 °C after DSC cycling.

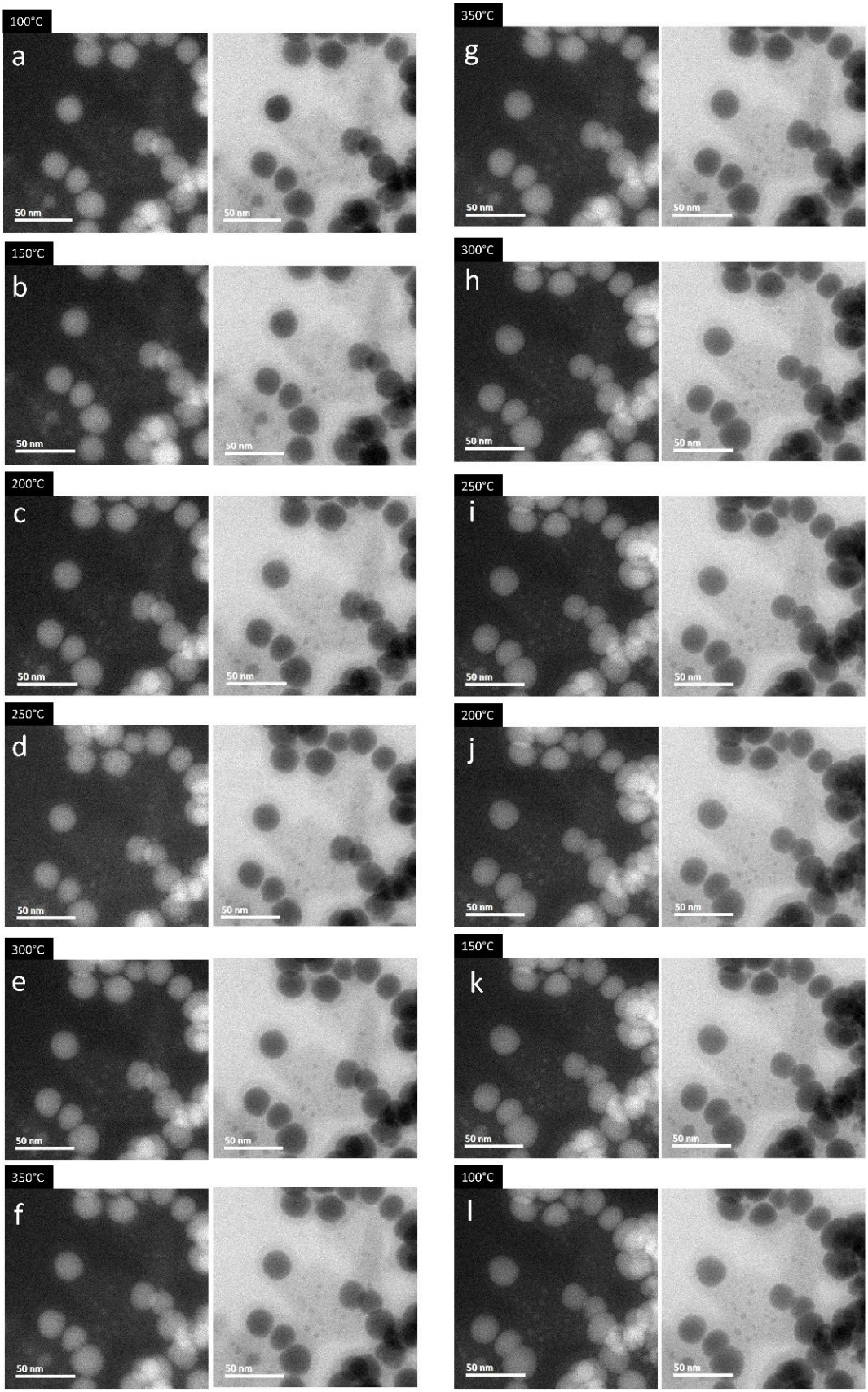

Figure S3. *In situ* STEM-HAADF and corresponding bright field STEM images of Bi@SiO_2 nanostructures during heating from 100 to 350 °C (left column) and cooling down (right column) under 760 Torr of argon at 10 °C min^{-1}.

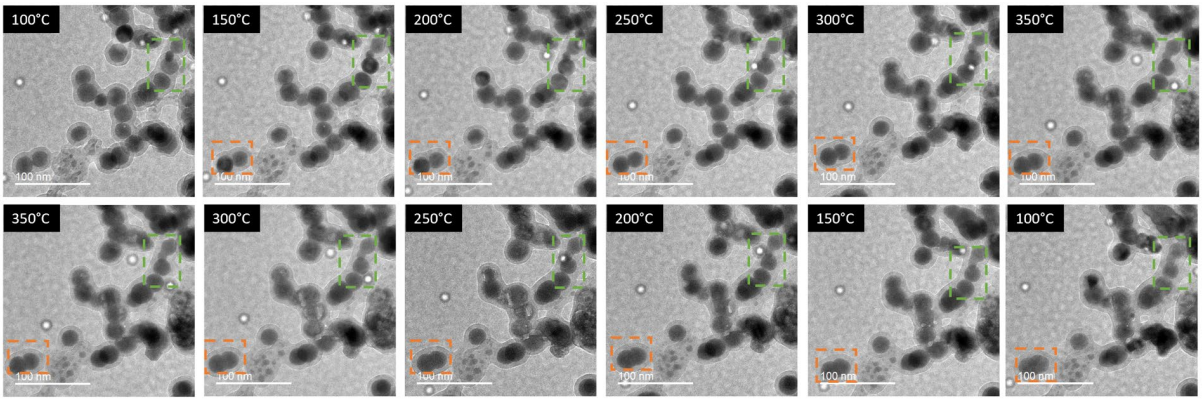

Figure S4. TEM images of Bi@SiO_2 nanostructures during heating from 100 to 350 °C (first row) and cooling (second row) under 760 Torr of argon at 10 °C min^{-1}. The samples was preheated at 100 °C for 2h. The orange rectangle shows two Bi cores embedded in the same silica shell and coalescing irreversibly. The green rectangle shows Bi cores that remain separated after cooling.

Figure S5. Optical image of Bi@SiO_2-Al sample.

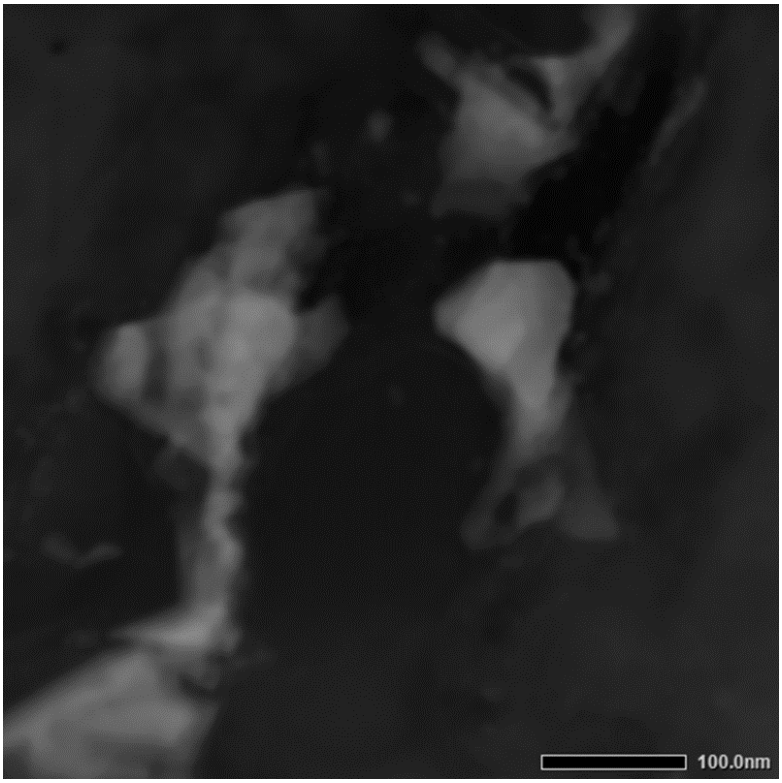

Figure S6. STEM-HAADF image of a Bi@SiO_2-Al nanocomposite, at 0.25 at. % of bismuth particles.